

Experimental testing of a solar air cavity-receiver with reticulated porous ceramic absorbers for thermal processing at above 1000 °C

Journal Article**Author(s):**

Patil, Vikas R.; Kiener, Fabio; Grylka, Adrian; [Steinfeld, Aldo](#) 

Publication date:

2021-01-15

Permanent link:

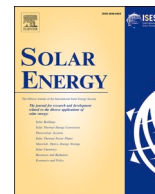
<https://doi.org/10.3929/ethz-b-000458501>

Rights / license:

[Creative Commons Attribution 4.0 International](#)

Originally published in:

Solar Energy 214, <https://doi.org/10.1016/j.solener.2020.11.045>



Experimental testing of a solar air cavity-receiver with reticulated porous ceramic absorbers for thermal processing at above 1000 °C

Vikas R. Patil, Fabio Kiener, Adrian Grylka, Aldo Steinfeld*

ETH Zurich, Department of Mechanical and Process Engineering, 8092 Zurich, Switzerland

ARTICLE INFO

Keywords:

Solar
Thermal
Concentrated
Volumetric
Receiver
Cavity
Process heat
High temperature

ABSTRACT

Concentrated solar energy can be used as the source of high-temperature heat for industrial processes, but the challenge is to design a solar receiver that can effect such a thermal conversion efficiently. This study reports on the engineering design and experimental testing of a 5 kW solar cavity-receiver containing a reticulated porous ceramic (RPC) structure that can absorb high-flux radiation volumetrically and heat up, by convection, an air flow serving as the heat transfer fluid. The thermal performance, characterized by the thermal efficiency and the air outlet temperature, was determined experimentally for four parameters, namely: RPC material (silicon-infused silicon carbide or SiSiC, alumina, and ceria), mean pore size (range 0.8–2.5 mm, corresponding to 10–30 pores per inch or PPI, at 0.90 porosity), solar concentration ratio (range 1965–3900 suns over a 4 cm-diameter cavity aperture, supplied by a high-flux solar simulator), and air mass flow rate (range 2–10 kg/h). Thermal efficiencies between 0.22 and 0.69 were obtained at steady-state air outlet temperatures ranging from 1160 to 450 °C. Larger pores enhance heat transfer while variable porosity across the RPC can reduce temperature gradients and potentially contribute to the design optimization. The highest efficiency of 0.69 was achieved by the SiSiC 10 PPI cavity at an air outlet temperature of 1133 °C and air mass flow rate of 9.9 kg/h. The solar receiver design proved to deliver a high-temperature air flow (>1000 °C) with a reasonably high thermal efficiency (>0.65).

1. Introduction

Several energy-intensive thermal and thermochemical processes of industrial interest proceed at high temperatures (>1000 °C) and are characterized by their concomitant emissions of vast amounts of greenhouse gases (GHG) and other pollutants, derived mainly from the combustion of fossil fuels for heat generation. Examples are found in the power generation sector (e.g. Brayton heat engines), in the mineral and metallurgical sector (e.g. calcination, carbothermic reduction, and recycling processes), and in the production of fuels and chemical commodities (e.g. reforming, gasification, and H₂O/CO₂ splitting cycles). For example, direct CO₂ emissions from the production of iron and steel accounted for 6–7% of the global GHG emissions in 2017, while cement production accounted for another 6–7% (International Energy Agency, 2020), highlighting the importance of decarbonizing these processes. The production of solar drop-in fuels for the aviation and shipping sectors can further avoid approximately 6% of the global GHG emissions (Eyring et al., 2005; Grote et al., 2014). Thus, GHG emissions can be significantly diminished and even eliminated by substituting fossil fuel

by concentrated solar energy as the source of high-temperature process heat, which can be delivered at large scale (>100 MW_{thermal}) by concentrating solar tower systems (Romero and Steinfeld, 2012). Only few stable heat transfer media are suitable for application at the pertinent temperatures, such as gases, supercritical fluids, liquid metals, and ceramic particles (Romero and González-Aguilar, 2017). If the application allows for an oxidizing atmosphere, air becomes an attractive heat transfer fluid (HTF). Despite its inferior heat transfer properties vis-à-vis other HTFs, especially its relatively low specific heat capacity, air has the advantage of being stable, safe, abundant, environmentally benign, and inexpensive. In addition, solar air receivers can be directly integrated with a thermocline-based heat storage system using a packed bed of rocks (Zanganeh et al., 2012), combined with a thermochemical heat storage system using for example the CuO/Cu redox cycle (Gigantino et al., 2020), enabling the round-the-clock delivery of heat at high temperatures for industrial applications. For these reasons, high-temperature solar receivers have predominantly used air as the HTF (Sedighi et al., 2019) and can be classified into tubular and volumetric (Ho, 2017). Solar tubular receivers use an array of opaque metallic or ceramic tubes exposed to concentrated solar radiation and

* Corresponding author.

E-mail address: aldo.steinfeld@ethz.ch (A. Steinfeld).

<https://doi.org/10.1016/j.solener.2020.11.045>

Received 7 August 2020; Received in revised form 9 November 2020; Accepted 16 November 2020

Available online 13 December 2020

0038-092X/© 2020 The Author(s). Published by Elsevier Ltd on behalf of International Solar Energy Society. This is an open access article under the CC BY

license (<http://creativecommons.org/licenses/by/4.0/>).

Nomenclature

c_p	specific heat capacity [J/kg/°C]
C	solar concentration ratio
HFSS	high-flux solar simulator
HTF	heat transfer fluid
I_{solar}	solar flux intensity [kW/m ²]
\dot{m}_{air}	mass flow rate of air across the receiver [kg/h]
PPI	pores per inch
P_{solar}	solar radiative power [kW]
RPC	reticulated porous ceramic
$T1$ to $T5$	temperatures on the RPC's outer periphery [°C]
SiSiC	silicon-infused silicon carbide
T	temperature [°C]
$T3_{\text{front}}$, $T4_{\text{front}}$	temperatures on the RPC's inner periphery in front of $T3$ and $T4$ [°C]
$T_{\text{air,out}}$	outlet air temperature [°C]
$T_{\text{pyrometer}}$	pyrometer temperature [°C]
η_{receiver}	thermal efficiency of the solar receiver [-]

carrying the HTF on the inside. They have a scalable modular design (multiple tubes) and can sustain high fluid pressures, but at the expense of design limitations imposed by the materials of construction of the tube such as the maximum operating temperature, thermal conductivity, resistance to thermal shocks, and inertness to oxidation by air. On the other hand, solar volumetric receivers use metallic or ceramic porous structures directly exposed to the incident concentrated solar radiation, enabling its penetration and absorption within the volume and not just on the exposed surface. This way, heat is efficiently transferred to the air flowing across the porous matrix. With proper design, the maximum solid and air temperatures can be achieved in the interior of the structure, which reduces re-radiation losses to the surroundings and the thermal loading on the solar receiver walls (Hoes et al., 2019; Luque et al., 2018). This phenomenon is typically described as the 'volumetric effect', wherein the temperature of the solid at the front (irradiated) side is lower than that of the air exiting the absorber at the rear.

The most important indicator of the thermal performance of the solar receiver is its thermal efficiency, η_{receiver} , which gives the conversion extent of the incident solar radiative energy into the sensible heat of the HTF. For a solar air receiver, it is defined as the ratio of enthalpy gain of air flowing across the receiver and the solar radiative power input P_{solar} :

$$\eta_{\text{receiver}} = \frac{\dot{m}_{\text{air}} \int_{T_{\text{air,in}}}^{T_{\text{air,out}}} c_p(T) dT}{P_{\text{solar}}} \quad (1)$$

where \dot{m}_{air} is the air mass flow rate, $T_{\text{air,in}}$ and $T_{\text{air,out}}$ are the inlet and outlet air temperature, and $c_p(T)$ is the temperature-dependent specific heat capacity of air.

Some of the earliest documented tests of solar volumetric air receivers were performed in the late 1970s (Battleson, 1981). Numerous experimental and numerical works have been carried out since then in pursuit of high η_{receiver} at high air outlet temperatures. Ávila-Marín (Ávila-Marín, 2011) provided a chronological review of volumetric receivers tested until 2010. Subsequent advances in volumetric receivers have been summarized in (Gomez-Garcia et al., 2016a; Ho, 2017; Ho and Iverson, 2014). A brief overview of solar volumetric receivers is provided from the point of view of absorber materials, operating pressure, absorber morphologies and incident solar flux intensity. In terms of materials, volumetric absorbers can be either metallic or ceramic. Metallic absorbers can provide stable operation under varying conditions owing to their high thermal conductivity, making them promising candidates for applications at up to 900 °C. Metallic absorbers have been tested experimentally with various morphologies, examples of which

include wire meshes (Ávila-Marín et al., 2018, 2014), open-cell foams (Albanakis et al., 2009), monolithic honeycombs (Pabst et al., 2017) and additively manufactured ordered structures (Capuano et al., 2017; Luque et al., 2018). As the industrial processes targeted by this study proceed at above 1000 °C, the following discussions will focus on ceramic absorbers. In terms of operating pressure, pressurized as well as atmospheric receivers have been tested. Several high-temperature volumetric receiver designs have used pressurized air with the aim to directly integrate with a Brayton power cycle, with air serving both as the HTF and working fluid (Sedighi et al., 2019). Examples are windowed air receivers containing Si₃N₄ and SiC foam absorbers, achieving a maximum η_{receiver} of 0.71 at 1050 °C and 5.2 bar pressure (Buck et al., 2002; Leuchsner, 1991; Pritzkow, 1991), and containing a ceramic pin based absorber, achieving a record high η_{receiver} of 0.80 at 1200 °C and 19.7 bar (Karni et al., 1997; Kribus et al., 2001). Windows are critical and troublesome components in scale-up designs because they must be relatively thin for minimum radiation attenuation yet strong and durable at high temperatures and pressures (Karni et al., 1998; Röger et al., 2006). An example of a windowless pressurized air receiver is a SiC cavity with an annular reticulated porous ceramic (RPC) foam-type absorber made of SiSiC, delivering air outlet temperatures exceeding 1200 °C and achieving a maximum η_{receiver} of 91% at 700 °C and 4 bar (Hischier et al., 2012; Pozivil et al., 2015). On the other hand, atmospheric pressure or 'open' air receivers draw ambient air directly into their porous absorbers. Open solar air receivers could facilitate the integration of solar heat into high-temperature processes without the limitations of pressurized receivers by decoupling the pressure-specific stage via an intermediate heat exchange stage and/or thermal energy storage stage using a HTF at ambient pressure. The use of solar receivers in such a configuration has been proposed by several recent studies, including for power generation via highly efficient combined cycle (topping air Brayton and bottoming steam Rankine) (Zaversky et al., 2020), gasification of carbonaceous waste (Parrodi et al., 2019), liquid fuel production via methane reforming (von Storch et al., 2016), calcination of limestone for cement production and reduction of metal ores (Nathan et al., 2019). In terms of absorber morphology, ceramic absorbers have been experimentally tested in various forms, examples of which include monolithic honeycombs (Agrafiotis et al., 2007; Gomez-Garcia et al., 2016b; Hoffschmidt et al., 1999; Li and Zhang, 2020), RPC structures (Chavez and Chaza, 1991; Mey-Cloutier et al., 2016; Wang et al., 2020; Zaversky et al., 2018), and additively manufactured ordered structures (Hoes et al., 2019). Of special interest are the RPC structures because of their efficient volumetric absorption and enhanced solid-fluid convective heat transfer, as demonstrated in high-temperature solar thermal and thermochemical applications (Buck et al., 1991; Chavez and Chaza, 1991; Fend et al., 2004; Furler et al., 2012; Marxer et al., 2017; Zaversky et al., 2019). The relevant heat transfer properties are thus the extinction coefficient and the convective heat transfer coefficient, which in turn depend on the porosity and pore size (or pore density, often expressed in pores per inch – PPI). In the pursuit of achieving the volumetric effect, numerous numerical and experimental studies have been undertaken to study the impact of porosity and pore size on the heat transfer within the RPCs (Haussener et al., 2010; Mey-Cloutier et al., 2016; Petrasch et al., 2008, 2007; Wang et al., 2020; Wu et al., 2011; Zaversky et al., 2018).

The conversion of concentrated solar radiation to heat at a given temperature is a function of the solar concentration ratio C , defined as the solar radiative flux intensity I_{solar} normalized over 1 kW/m² (i.e. 1 sun). Current commercial solar tower systems are mainly designed for $C < 1000$ suns (Blanco and Miller, 2017) averaged over the solar receiver's aperture, delivering process heat usually at below about 600 °C for driving steam-based Rankine cycles. Most of the experimental studies on volumetric receivers have also used mean $C < 1000$ suns. In recent years, values of $C > 2500$ suns have been demonstrated at pre-commercial scale using a densely-packed heliostat field (Romero et al., 2019) and/or secondary optics (Pozivil et al., 2015), enabling the

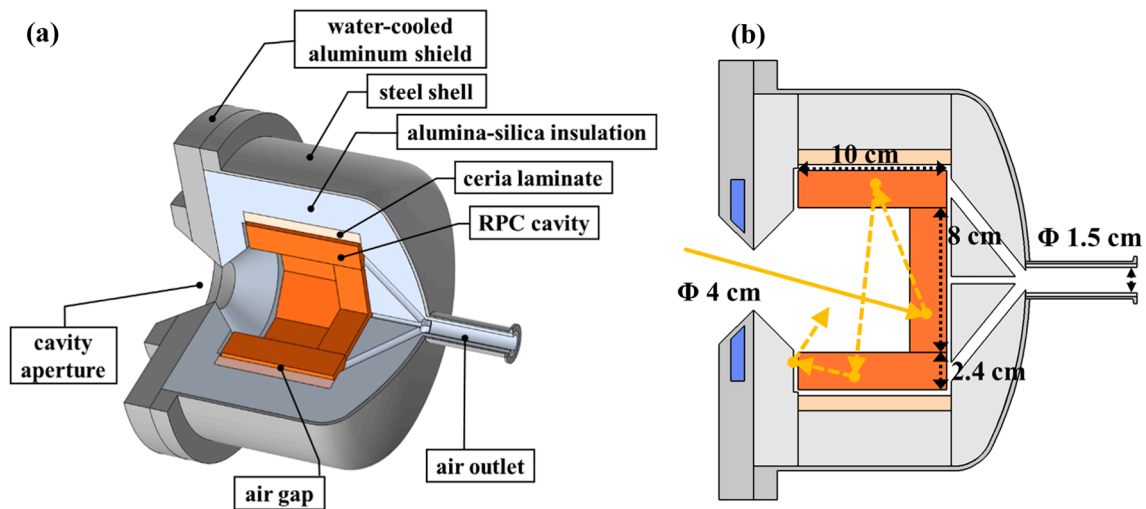


Fig. 1. (a) 3-D cut-section of the solar receiver, (b) vertical cross-section marked with main dimensions, and displaying radiative propagation of a generic incident sunray (solid line) and its subsequent scattering or re-emission (dashed lines).

delivery of heat at temperatures exceeding 1000 °C.

In view of the potential of open volumetric solar receivers, and the significance of the RPC properties for obtaining superior thermal performance, this study aims to demonstrate a proof-of-concept of a solar cavity-receiver compact design featuring RPC bricks as volumetric absorbers and air as HTF, and to investigate the influence of various design and operational parameters. Modular arrays of a scaled-up version of such a solar receiver concept are envisaged on top of a solar tower with secondary optics for high solar concentration ratios, to drive thermal and thermochemical processes highlighted in the preceding discussion that operate at close to or above 1000 °C. Results of experimental testing of the lab-scale solar receiver are presented, using RPCs of different materials and mean pore size, exposed directly to thermal radiation generated by a high-flux solar simulator of varying flux intensities and subjected to an air flow of varying mass flow rates. The dependent variable of primary interest is the air outlet temperature under steady-state conditions. The significance of these experimental parameters is explained as follows.

RPC material – High surface absorptivity in the visible and IR range of the spectrum is important for maximizing the absorption of incident solar radiation and high-temperature radiative emission. High thermal conductivity is important for homogenizing the temperature across the RPC structure by mitigating hotspots and associated flow instabilities. Three RPC materials were investigated: silicon-infused silicon carbide (SiSiC), alumina (Al_2O_3) and ceria (CeO_2). SiSiC has a relatively high absorptivity and thermal conductivity (Gianella et al., 2012). Alumina has a significantly lower absorptivity and thermal conductivity compared to SiSiC, but it has a high maximum service temperature in air of about 1750 °C (Gianella et al., 2012), which is a favorable attribute for high-temperature absorbers. Surface absorptivity of ceria is high at

high temperatures due to change in non-stoichiometry (Ackermann et al., 2017), while its thermal conductivity is even lower than that of alumina.

RPC mean pore size – Porosity and pore size can significantly affect the interplay between radiative and convective heat transfer. There is a general consensus in the literature that higher foam porosity (approaching 0.90) results in higher receiver efficiency owing to enhanced radiation heat transfer by enabling deeper radiative penetration (Kribus et al., 2014; Wang et al., 2020; Wu et al., 2011; Zaversky et al., 2018). Accordingly, a porosity of ~ 0.90 was chosen for the various RPC samples tested in this study. Large pores (mean pore diameter ~ 4 mm) absorb the incident solar radiation more uniformly within the RPC volume (Kribus et al., 2014), whereas smaller pores lead to better convective heat transfer between the RPC and the air (Mey-Cloutier et al., 2016; Wang et al., 2020; Zaversky et al., 2018), although additional factors play a role too, including flux intensity and direction of incident radiation, spectral selectivity and thermal conductivity of RPC material, and air mass flow rate. The optimum pore size is therefore expected to be a gradient from large to small pores in the direction of incident radiation (Kribus et al., 2014). While such gradients are not feasible with conventional foam fabrication methods, this study investigated RPCs with uniform but different pore sizes in the range 2.5–0.8 mm, corresponding to pore densities between 10 and 30 PPI, as the basis for validating a detailed heat transfer and fluid flow model of the solar receiver. The validated model is expected to deliver, among other things, an optimum pore size distribution for achieving maximum η_{receiver} .

Radiative flux intensity – This study used I_{solar} values ranging between 1965 and 3900 kW/m^2 (averaged over the receiver aperture) – supplied in this case by a high-flux solar simulator.

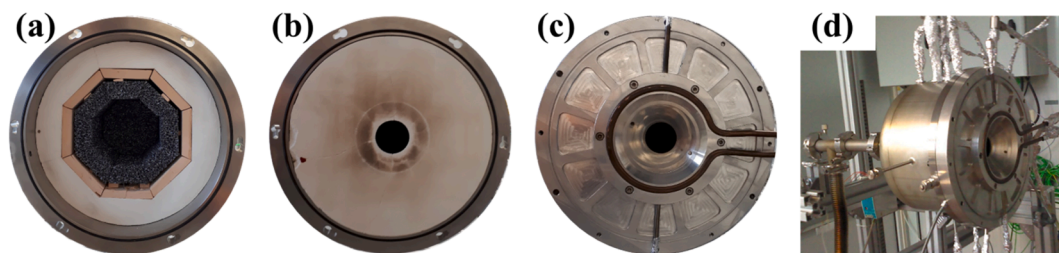


Fig. 2. Photographs of the solar receiver assembly: (a) cavity front with RPC bricks (SiSiC 10 PPI) lined with ceria laminate and alumina-silica insulation. (b) Cavity front closed by alumina-silica insulating disk with 4 cm-diameter open aperture. (c) Water-cooled aluminum shield to protect from spilled radiation. (d) Fully assembled solar receiver with cooling water connections at the front, thermocouple ports along the lateral steel shell and the air outlet connection at the rear.

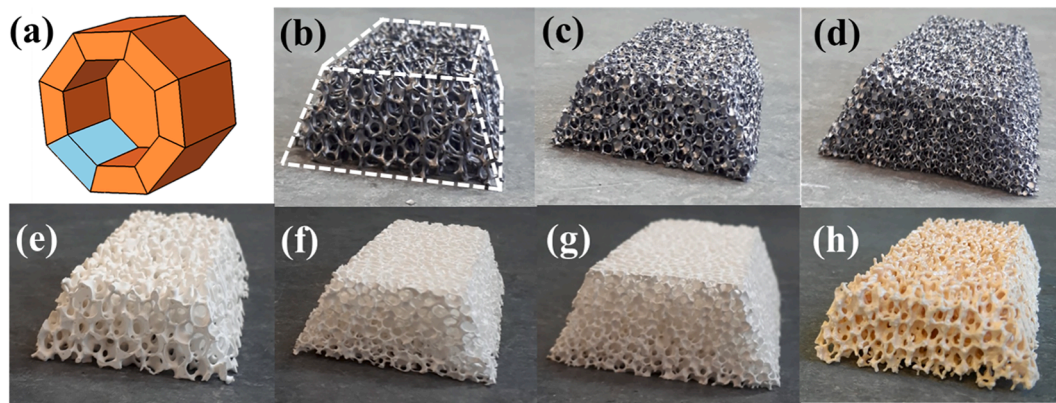


Fig. 3. (a) 3D schematic of the RPC cavity with one of the trapezoidal RPC bricks highlighted in blue. Photograph of one such trapezoidal RPC brick from the seven different cavities tested: (b) SiSiC 10 PPI (dashed white lines outlining the trapezoidal shape), (c) SiSiC 20 PPI, (d) SiSiC 30 PPI, (e) alumina 10 PPI, (f) alumina 20 PPI, (g) alumina 30 PPI, (h) ceria 10 PPI. (For interpretation of the references to colour in this figure legend, the reader is referred to the web version of this article.)

Air mass flow rate – The resulting $T_{\text{air,out}}$ and η_{receiver} are strongly dependent on the air mass flow rate across the RPCs, which was varied between 2 and 10 kg/h.

The following sections describe in detail the solar receiver design, materials and methods used for its testing, and its thermal performance.

2. Solar receiver design

Fig. 1 shows: a) a cut-section of the 3-D geometry of the solar receiver, and b) its main dimensions and radiative propagation of a generic incident sunray across the cavity. Fig. 2 shows photographs outlining the various assembly stages of the solar receiver. It comprises an axisymmetric cavity constructed as an assembly of eight trapezoidal RPC bricks forming an octagon and an octagonal RPC brick at the rear end of the cavity (Fig. 2a). The octagonal shape was chosen considering the modularity and structural stability of the cavity made out of an array of bricks at the given size scale. This modular arrangement facilitates scale-up by increasing the number of bricks while maintaining thermo-mechanical stability of individual bricks. The cavity front is closed by an alumina-silica insulating disk with a 4 cm-diameter aperture for the

access of concentrated solar radiation (Fig. 2b). With this enclosure-type arrangement, the RPC cavity is directly exposed to high-flux solar radiation, enabling efficient radiative absorption by multiple internal reflections and approaching a blackbody absorber. Its apparent absorptance, calculated by the Monte Carlo ray-tracing technique, is 0.995. The aperture is windowless, i.e. it is open to the surroundings at the front for the access of ambient air used as the HTF. A layer of ceria laminate insulation surrounds the length of the RPC cavity, which is further bounded by alumina-silica insulation blocks. A 5 mm gap is maintained between the RPC bricks and the insulation walls using spacers. The air gap, being directly connected to the channels leading to the receiver outlet, creates a pressure difference across the thickness of the RPC which facilitates uniform air flow especially in the radial direction, consequently improving the convective heat transfer between the RPC and the air. Air enters the cavity from the front, flows across the RPC structure, and exits through five channels through the ceramic insulation which merge into an outlet axial alumina pipe (Alsint 99) at the rear of the cavity. This assembly is enclosed in a stainless steel vessel. An internally water-cooled aluminum shield around the aperture protects the setup from spilled radiation (Fig. 2c).

Table 1

Morphological, optical and thermal properties of the seven RPCs tested in this work, relevant for high-flux, high-temperature radiative and convective heat transfer.

RPC material	Ceria	SiSiC			Alumina			References
Nominal pore density (PPI)	10	10	20	30	10	20	30	ceria: (Ackermann et al., 2017); SiSiC and alumina: manufacturer.
Macro porosity* (–)	0.83	0.90	0.91	0.87	0.90	0.91	0.87	
Strut porosity* (–)	0.26	0	0	0	0.30	0.30	0.30	
Dual-scale porosity* (–)	0.87	0.90	0.91	0.87	0.93	0.94	0.91	Calculated using correlations in (Ackermann et al., 2017)
Mean pore diameter (mm)	~2.3	~2.5	~1.2	~0.8	~2.5	~1.2	~0.8	
Specific surface area (m ² /m ³)	842	778	1537	2412	778	1537	2412	
Extinction coefficient (m ⁻¹)	301	247	480	804	247	480	804	
Spectral hemispherical reflectivity (–)	0.30–0.90 in visible spectrum	0.09–0.03 @ 1.0–1.4 μm and ~800–1300 °C			0.85–0.40 @ 0.88 μm and ~1000–2000 °C			(Ackermann and Steinfeld, 2017; Potamias et al., 2019)
Solid thermal conductivity (Wm ⁻¹ K ⁻¹)								(Ackermann et al., 2017; Ortona et al., 2014; Purdue University. Thermophysical Properties Research Center, 1967)
@500 °C	5.13	~60			~10.89			
@1000 °C	1.82	~42			~6.35			
@1500 °C	0.83	~38			~7.43			
Effective thermal conductivity (Wm ⁻¹ K ⁻¹)	@0.87 porosity (10 PPI):	@0.90 porosity (10 PPI):			@0.93 porosity (10 PPI):			Calculated using correlation in (Ackermann et al., 2017)
@500 °C	~0.2654	~1.4110			~0.1602			
@1000 °C	~0.1736	~1.0430			~0.1571			
@1500 °C	~0.1672	~0.9906			~0.2018			

*Macro porosity includes only the voids formed by foam cells and macro-pores; strut porosity results from voids left behind by incineration of the polymer foam template and micro-pore forming additives, if any; dual-scale porosity includes the macro and strut porosity. For details, see (Ackermann et al., 2017). SiSiC has zero strut porosity due to infusion of Si in the strut voids.

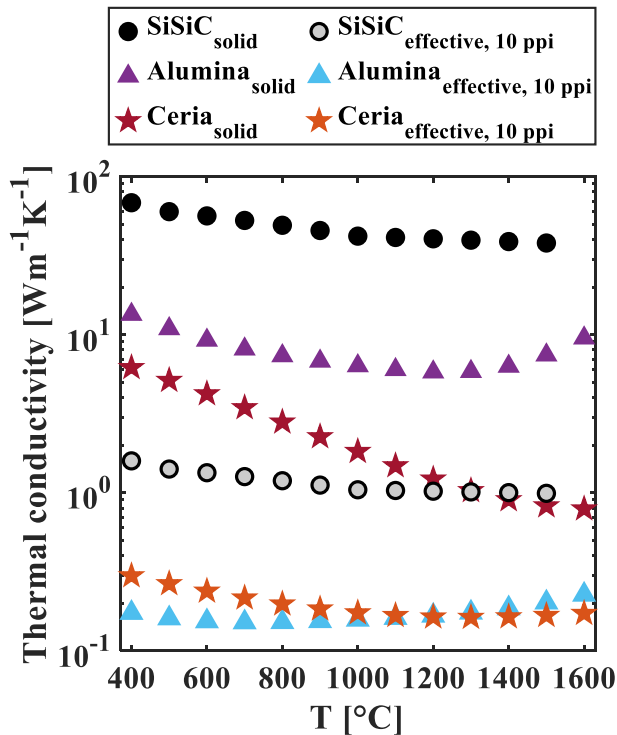


Fig. 4. Solid thermal conductivities of SiSiC, alumina and ceria, and effective thermal conductivities of their 10 PPI RPCs as a function of temperature, plotted on a logarithmic scale to highlight significant differences.

RPC materials – Correlations between RPC mean pore diameter, porosity and nominal pore density, determined by processing the exact 3D digital geometry of the RPC obtained by tomographic scans (Ackermann et al., 2017), were applied in this study. As the porosity of all the RPCs was nearly the same ($\sim 90\%$), the pore density of an RPC, expressed in pores per inch (PPI), has been used throughout this work to identify the pore size. The SiSiC and alumina RPCs have nominal pore densities of 10, 20 and 30 PPI each, which were the standard foam sizes available at their commercial manufacturer (EngiCer SA, Switzerland). The ceria RPC with 10 PPI was manufactured in-lab using the replica method and was also included because it has been studied extensively

for thermochemical applications (Furler et al., 2012). Fig. 3 shows the seven different RPCs tested. Table 1 provides their morphological, optical and thermal properties relevant for high-flux, high-temperature radiative and convective heat transfer based on manufacturer data and correlations from literature. Fig. 4 plots the thermal conductivity of solid SiSiC, alumina and ceria as well as effective thermal conductivity of their 10 PPI RPCs as a function of temperature. The solid thermal conductivity of SiSiC, and hence the effective thermal conductivity of its RPC, are significantly higher than those of alumina and ceria, which makes an interesting case for comparative study.

3. Experimental set-up

Fig. 5 depicts the scheme of the experimental setup. Experimentation was carried out at the ETH's high-flux solar simulator (HFSS): an array of seven high-pressure Xe arcs, each close-coupled to ellipsoidal reflectors, supplied a beam of concentrated thermal radiation mimicking the radiative heat transfer characteristics of highly concentrating solar systems. P_{solar} was measured by placing a water-cooled calorimeter at the same location in the solar simulator as the solar receiver, before the experimental runs. The calorimeter is a well-insulated cavity with the same aperture diameter and front conical section as the solar receiver. Its inner surfaces are lined with an absorbent-coated, coiled copper tube carrying cooling water. With an apparent absorptance of 0.995 (determined by ray-tracing simulations), the radiant power P_{solar} from the lamps entering through the calorimeter aperture is equal to the enthalpy gain of the cooling water, calculated by measuring the mass flow rate and increase in water temperature. During the experimental runs, the same P_{solar} entered the solar receiver through its aperture. The windowless aperture also served as an inlet for ambient air, suctioned into the cavity by a downstream vacuum pump (Becker AG, VASF 1.80/2). The air mass flow rate \dot{m}_{air} was controlled by varying the suction pressure generated by the vacuum pump using its in-built variable frequency drive. Five B-type sheathed thermocouples (Omega Engineering Ltd.), T1-T5, measured temperatures of the RPC structure at its outer periphery. Air temperature at the outlet was measured by a K-type sheathed thermocouple (Omega Engineering Ltd.), $T_{\text{air,out}}$, located 4 cm downstream of the merger point of the five outlet channels from the cavity and roughly at the center of the cross-section of the outlet pipe (see Fig. 5). A second, similar thermocouple placed at the same axial location but nearly touching the outlet wall, verified that there was no significant difference in $T_{\text{air,out}}$ ($<5\%$ relative at low flow rates, $<1\%$ at

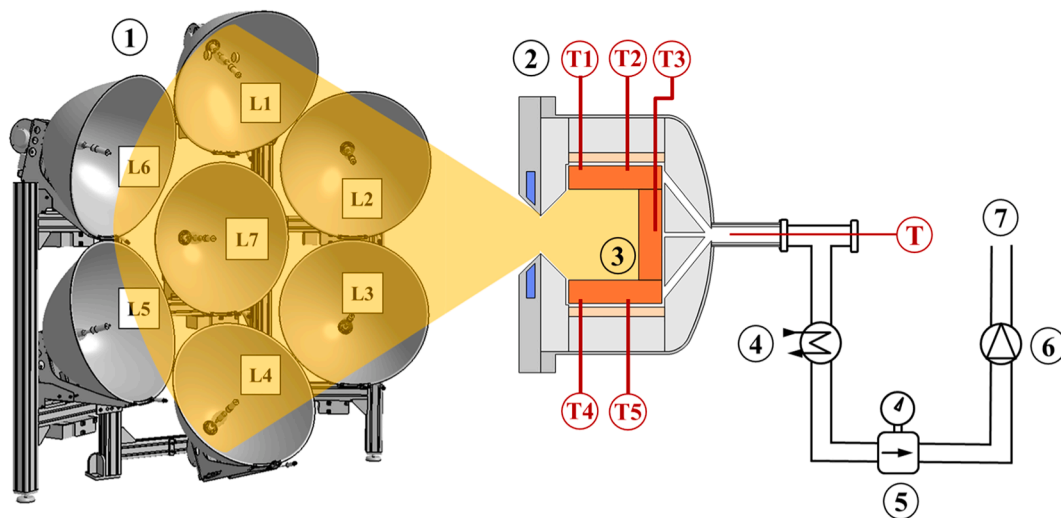
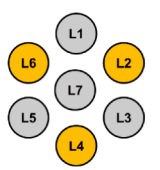
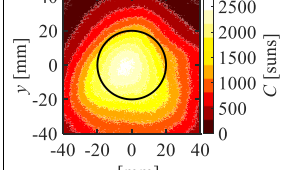
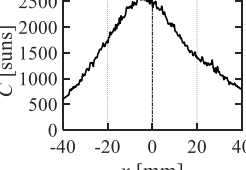
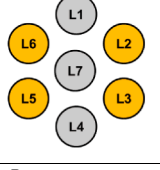
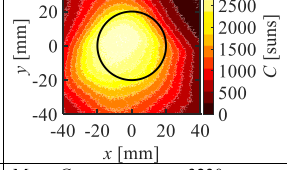
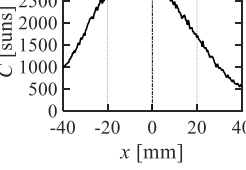
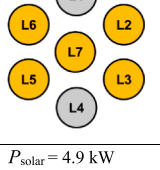
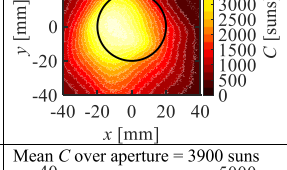
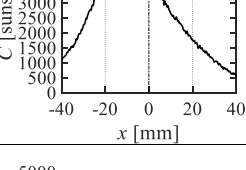
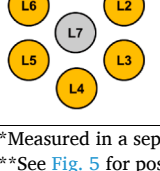
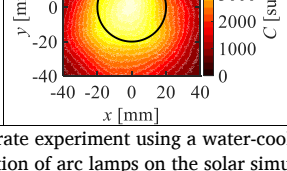
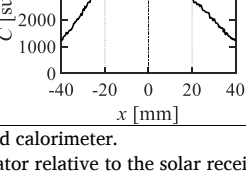


Fig. 5. Schematic of the experimental setup: (1) HFSS with seven Xe-arc lamps (L1-L7) coupled to ellipsoidal reflectors, (2) solar receiver, (3) RPC cavity, (T1-T5) five thermocouples at the RPC outer periphery, (T) thermocouple at air outlet, (4) water-cooled heat exchanger, (5) air mass flow meter, (6) vacuum pump, (7) laboratory gas exhaust. Relative dimensions between the HFSS and the solar receiver are not to scale.

Table 2
Details of the four radiative power levels supplied to the solar receiver by the HFSS.

P_{solar} at aperture*, arc lamps used**	C distribution on aperture plane*** (40 mm diameter aperture circled)	C distribution along x at y = 0 (±20 mm zone denotes aperture)
$P_{\text{solar}} = 2.5 \text{ kW}$ 	Mean C over aperture = 1965 suns 	
$P_{\text{solar}} = 3.1 \text{ kW}$ 	Mean C over aperture = 2475 suns 	
$P_{\text{solar}} = 4.1 \text{ kW}$ 	Mean C over aperture = 3230 suns 	
$P_{\text{solar}} = 4.9 \text{ kW}$ 	Mean C over aperture = 3900 suns 	

*Measured in a separate experiment using a water-cooled calorimeter.
**See Fig. 5 for position of arc lamps relative to the solar receiver.
***Measured in a separate experiment on a Lambertian target using a camera from the lamp side.

high flow rates) across the cross-section at the given location. This radial uniformity in $T_{\text{air,out}}$ could be explained by the small cross-section of the outlet pipe (1.5 cm internal diameter) and good mixing as hinted by high values of Reynolds number (in the range 1500–5000, depending on the flow rate) calculated using measured mass flow rate and $T_{\text{air,out}}$. In selected experimental runs, two S-type thermocouples (TC Direct, Pt/Pt-Rh10%) were placed on the RPC's inner periphery in front of thermocouples T_3 and T_4 to examine the temperature gradient across the RPC thickness. An infrared pyrometer (Omega Engineering Ltd., iR2C) targeting the open aperture was also installed to measure the effective cavity temperature, but it was applied for the SiSiC cavity only because reflected radiation contaminated the measurements for the alumina and ceria cavities. The air's sensible heat was not utilized. Instead, the heated air was cooled down to below 40 °C by a water-cooled shell-and-tube heat exchanger in order to stay below the maximum working temperatures of the air mass flow meter (Endress + Hauser AG, t-mass A150) and vacuum pump.

Parameters – Every experimental run was defined by four parameters: RPC material, RPC mean pore diameter, mean C over aperture, and \dot{m}_{air} . The three former were fixed for each experimental run while \dot{m}_{air} was varied over the range 2–10 kg/h in steps of roughly 0.75 kg/h during a single run. Thus, at a given \dot{m}_{air} , the steady-state $T_{\text{air,out}}$ was recorded as the quantity of primary interest. The (quasi) steady-state is defined as the first time instance when a change of < 1% in $T_{\text{air,out}}$ is recorded relative to its value during the last 5 min. Using different combinations of the arcs, four values of P_{solar} were applied: 2.5, 3.1, 4.1 and 4.9 kW. The corresponding mean values of C over the aperture were: 1965, 2475,

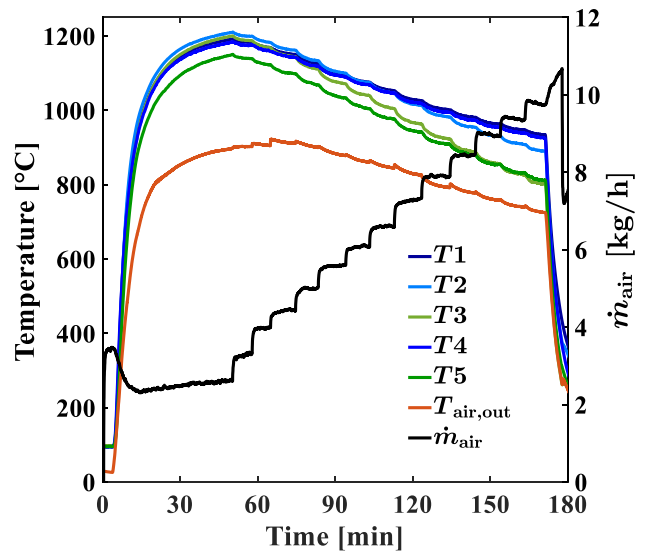


Fig. 6. Temporal variation of temperatures (left axis) and air mass flow rate (right axis) across the receiver over the course of a representative experimental run. Parameters: SiSiC 20 PPI cavity with $C = 2475$ suns.

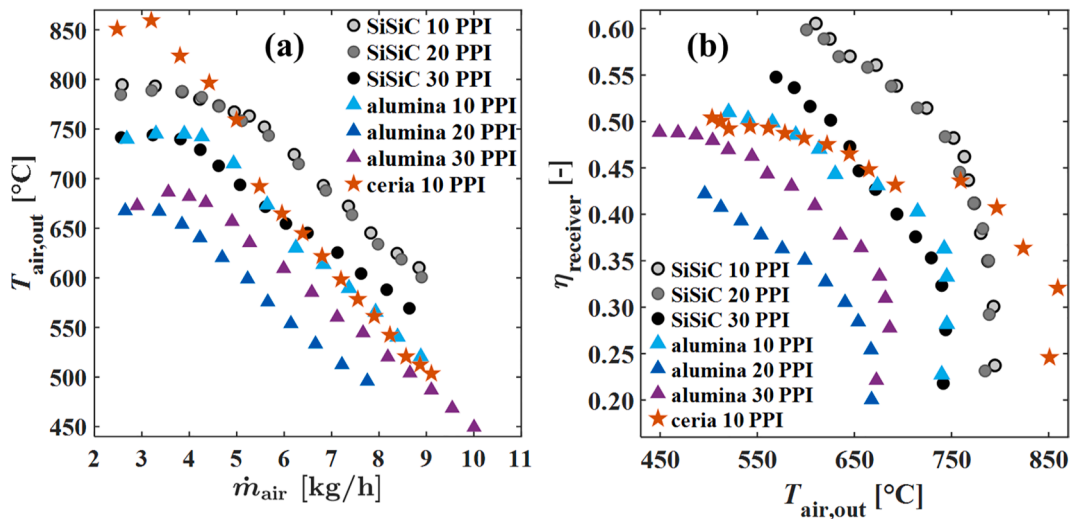


Fig. 7. Thermal performance of the seven RPC cavities, each tested at $C = 1965$ suns ($P_{solar} = 2.5$ kW): (a) steady-state $T_{air,out}$ as a function of \dot{m}_{air} (maximum error: ± 6 °C), (b) $\eta_{receiver}$ as a function of steady-state $T_{air,out}$ (maximum error: ± 0.04).

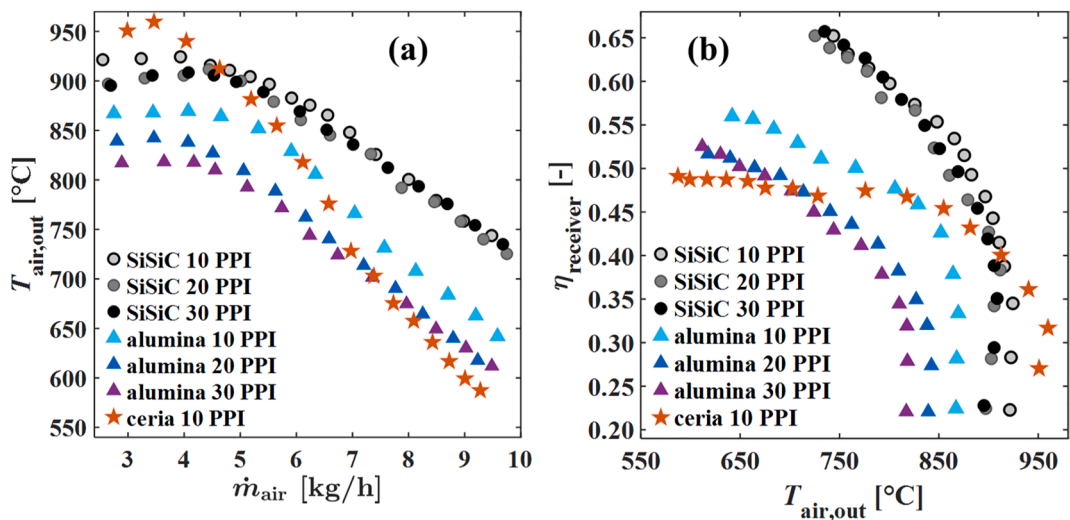


Fig. 8. Thermal performance of the seven RPC cavities, each tested at $C = 2475$ suns ($P_{solar} = 3.1$ kW): (a) steady-state $T_{air,out}$ as a function of \dot{m}_{air} (maximum error: ± 7 °C), (b) $\eta_{receiver}$ as a function of steady-state $T_{air,out}$ (maximum error: ± 0.04).

3230 and 3900 suns, respectively. Reproducibility of $T_{air,out}$ measurements was confirmed by repeating one of the experimental runs, namely SiSiC 30 PPI cavity with 3.1 kW power input (Appendix A). Calorimeter measurements were also repeated to verify P_{solar} reproducibility (for $\eta_{receiver}$ calculation), yielding measurements within a maximum error of 0.17 kW ($< 6.8\%$ of P_{solar}), based on instrumentation accuracy (Appendix B). The HFSS delivers stable steady-state radiative fluxes at fixed directional distributions, enabling reproducibility of the experimental boundary conditions. Table 2 shows the four combinations of HFSS arc lamps used and their corresponding radiative power and flux intensity distribution at the aperture plane.

4. Results and discussion

The course of a representative experimental run is plotted in Fig. 6. The experiment was started by igniting the relevant number of arcs of the HFSS while flowing air through the receiver at the minimum possible \dot{m}_{air} (~ 2.5 kg/h) to accelerate the heat up rate. Following an initial rapid rise, the temperature of the RPC cavity ($T1-T5$) and air at the receiver outlet ($T_{air,out}$) reached the first (quasi) steady-state at around 50 min

from the start. \dot{m}_{air} was then incremented in steps of ~ 0.75 kg/h, waiting long enough at each flow rate step to ensure that the quasi-steady-state condition was fulfilled for $T_{air,out}$. As expected, $T_{air,out}$ decreased with increasing \dot{m}_{air} . At around 10 kg/h, the experiment was completed by switching off the HFSS and maintaining the same air flow rate to facilitate cool down. Typically, $T1-T5$ were higher than $T_{air,out}$ by 200–400 °C, depending on the RPC material, pore density, and C . Despite being located symmetrically on the vertical cross-section of the solar receiver, readings of thermocouples T2 and T5 differed by up to 150 °C in some cases. Factors that may have influenced this data include: uneven irradiation of the cavity from the arcs of the HFSS, uncertainty of contact between the thermocouple tip and the RPC due to thermal expansion, and buoyancy effects.

Figs. 7–10 display the thermal performance of the seven different RPC cavities at the four C inputs: 1965, 2475, 3230 and 3900 suns. In each figure, part (a) plots the steady-state $T_{air,out}$ as a function of \dot{m}_{air} , while part (b) plots the $\eta_{receiver}$ as a function of the steady-state $T_{air,out}$ (following Eq. 1). The seven RPC cavities tested are denoted by distinct marker types in each figure. Maximum errors in $T_{air,out}$ and $\eta_{receiver}$, based on error propagation of associated instruments (see Appendix B),

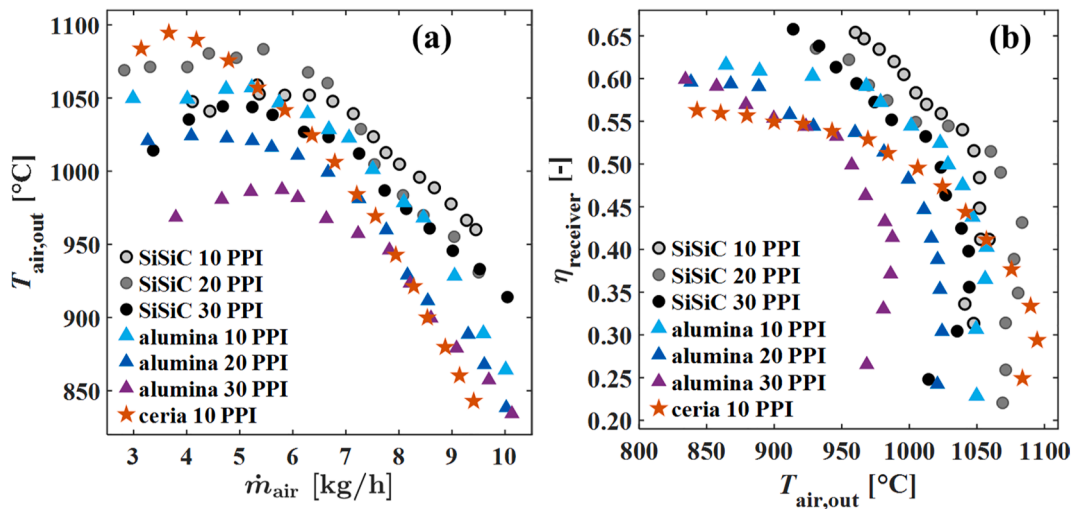


Fig. 9. Thermal performance of the seven RPC cavities, each tested at $C = 3230$ suns ($P_{solar} = 4.1$ kW): (a) steady-state $T_{air,out}$ as a function of \dot{m}_{air} (maximum error: ± 8 °C), (b) $\eta_{receiver}$ as a function of steady-state $T_{air,out}$ (maximum error: ± 0.04).

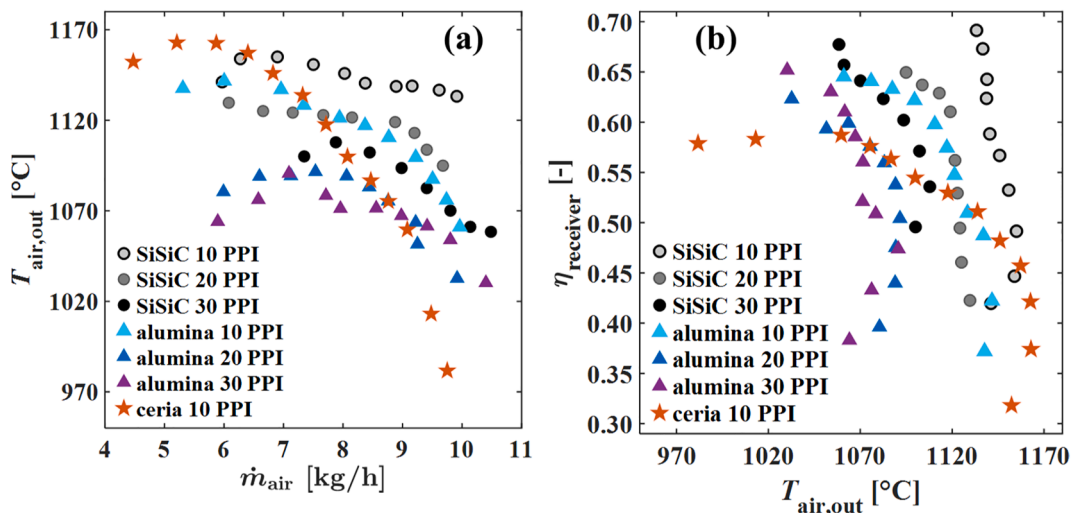


Fig. 10. Thermal performance of the seven RPC cavities, each tested at $C = 3900$ suns ($P_{solar} = 4.9$ kW): (a) steady-state $T_{air,out}$ as a function of \dot{m}_{air} (maximum error: ± 10 °C), (b) $\eta_{receiver}$ as a function of steady-state $T_{air,out}$ (maximum error: ± 0.04 °C).

are stated in the figure captions. For all runs, the steady-state $T_{air,out}$ decreases with increasing \dot{m}_{air} (part(a) of Figs. 7-10). Higher mass flow rates, hence higher interstitial velocities lead to better heat transfer between the RPC and the air, which in turn reduces the steady-state temperature attained by the RPC itself, and hence by the air. The steady-state $T_{air,out}$ at a given \dot{m}_{air} increases with P_{solar} , which is a direct consequence of increasing C (part(a) of Figs. 7-10). $\eta_{receiver}$ decreases with $T_{air,out}$ (part(b) of Figs. 7-10). This is because higher $T_{air,out}$ values result from higher RPC temperatures, which lead to higher radiative heat losses through the aperture and higher conductive heat losses through the thermal insulation, thus decreasing the $\eta_{receiver}$. The steep drop in $\eta_{receiver}$ above a certain $T_{air,out}$, as observed in each case, is indicative of increasing radiative heat losses, which scale with the fourth power of temperature. An additional common trend is the slight increase in $T_{air,out}$ with increase in \dot{m}_{air} for the first few \dot{m}_{air} data points (each experiment was started with the lowest \dot{m}_{air}), attributed to the transient heating of the insulating walls at the start of the experiment, as confirmed by repeating one of the experiments with a longer heat-up time before recording the first $T_{air,out}$ (Appendix A). This transient phenomenon does not affect the comparative analysis, as each experiment followed the same procedure.

For $C = 1965$ suns (Fig. 7(a)), $T_{air,out}$ ranged from about 850 to 450 °C over \dot{m}_{air} of 2.5 to 10 kg/h. For the same PPI, SiSiC cavities delivered higher temperatures than their alumina counterparts by about 45–140 °C, depending on PPI and \dot{m}_{air} , which corresponds to a relative difference of about 8–23%. Within the same material SiSiC, 10 PPI and 20 PPI cavities performed similarly and better (i.e. delivered higher $T_{air,out}$) than the 30 PPI under same operating conditions. For alumina, the 10 PPI cavity delivered the highest $T_{air,out}$, followed by 30 PPI and then 20 PPI cavities under same operating conditions. For ceria, the 10 PPI cavity achieved the highest $T_{air,out}$ among all the cavities, 860 °C at $\dot{m}_{air} = 3.2$ kg/h, but dropped sharply below $T_{air,out}$ of all SiSiC cavities with increasing \dot{m}_{air} . The ceria 10 PPI cavity had mm-scale gaps between adjacent RPC bricks at some locations because of imperfections in machining the bricks, which presumably led to the air bypassing parts of the RPC structures. Fig. 7(b) reflects this trend, wherein $\eta_{receiver}$ values of ceria 10 PPI change abruptly going from high $T_{air,out}$ (low \dot{m}_{air}) to low $T_{air,out}$ (high \dot{m}_{air}). In terms of $\eta_{receiver}$ (Fig. 7(b)), the highest $\eta_{receiver}$ value for every cavity is obtained at the lowest $T_{air,out}$ (i.e. highest \dot{m}_{air}), which drops sharply with increasing $T_{air,out}$ (i.e. decreasing \dot{m}_{air}) thereafter. At lower \dot{m}_{air} , the pore-scale Reynolds number is also lower and in the range

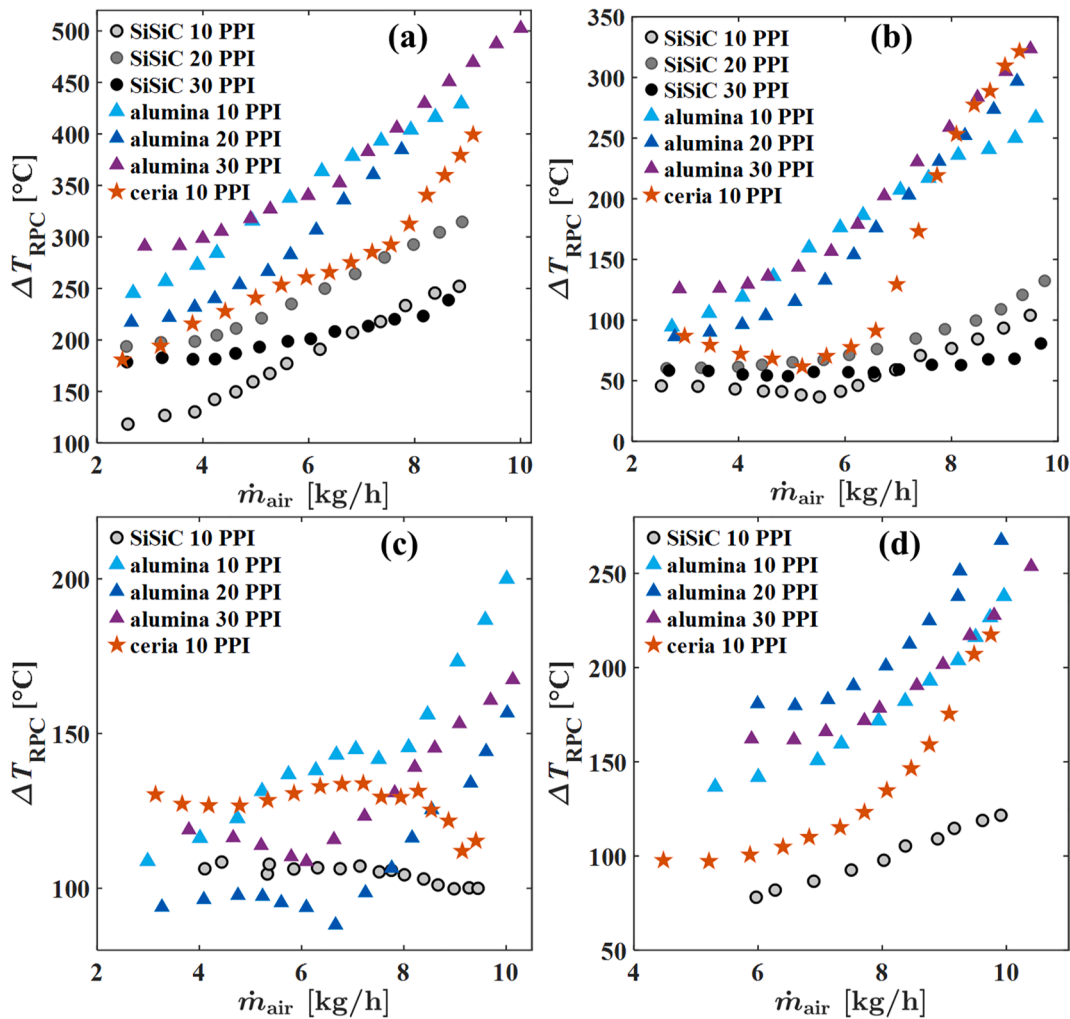


Fig. 11. Maximum difference between steady-state temperatures measured at five locations on the outer periphery of the RPC cavity (see *T1-T5* in Fig. 5) as a function of \dot{m}_{air} , for the seven different RPC cavities tested with $C =$ (a) 1965, (b) 2475, (c) 3230 and (d) 3900 suns. Values for SiSiC 20 and 30 PPI in (c) and (d) are omitted due to thermocouple malfunction.

5–200 at most locations in the RPC (estimated by CFD modeling), leading to poorer convective heat transfer between the RPC and the air. At higher $T_{\text{air,out}}$, the cavity loses significant portions of the absorbed P_{solar} via radiative emission through the open aperture and conduction through the insulation walls. The SiSiC 10 PPI cavity achieved the highest η_{receiver} of 0.61 at $T_{\text{air,out}} = 610$ °C and $\dot{m}_{\text{air}} = 8.8$ kg/h. At the highest $T_{\text{air,out}}$, η_{receiver} values were between 0.25 and 0.20 for all cavities because of the significant heat losses. Note that the η_{receiver} profile arches back slightly due to the aforementioned effect of transient heating of the insulation walls at the start of the experiment, which limited the value of steady-state $T_{\text{air,out}}$ achieved at the lowest \dot{m}_{air} .

For $C = 2475$ suns (Fig. 8(a)), $T_{\text{air,out}}$ ranged from 960 to 587 °C over $\dot{m}_{\text{air}} = 2.6$ to 9.8 kg/h. Most notably, the ceria 10 PPI cavity spanned this entire range of $T_{\text{air,out}}$, starting with the highest values among all the cavities at low \dot{m}_{air} and ending with the lowest $T_{\text{air,out}}$ at the highest \dot{m}_{air} . As discussed in the previous section, this behavior may be linked to air bypassing parts of the RPC structure. SiSiC cavities achieved higher temperatures than corresponding alumina cavities of the same PPI. In fact, all three SiSiC cavities, irrespective of pore size, achieved nearly the same $T_{\text{air,out}}$ at each \dot{m}_{air} (as seen from their overlapping plots), while also distinctly outperforming all the three alumina cavities. Within the alumina cavities, 10 PPI achieved the highest temperatures. At lower \dot{m}_{air} , alumina 20 PPI showed higher temperatures than 30 PPI, but this difference diminished with increasing \dot{m}_{air} . The discussion of η_{receiver}

(Fig. 8(b)) follows similarly to that of Fig. 7(b). The highest η_{receiver} value of about 0.66 was achieved by all the three SiSiC cavities, which performed similarly to each other, at $T_{\text{air,out}} \approx 730$ °C and $\dot{m}_{\text{air}} \approx 9.7$ kg/h. At the highest $T_{\text{air,out}} = 960$ °C, η_{receiver} approached 0.31.

For $C = 3230$ suns (Fig. 9(a)), $T_{\text{air,out}}$ ranged from 1095 to 834 °C over \dot{m}_{air} of 2.8 to 10.1 kg/h. Similar to the experiments of Fig. 7 and Fig. 8, the ceria 10 PPI cavity achieved higher $T_{\text{air,out}}$ than any other cavity and dropped steeply across $T_{\text{air,out}}$ values of all other cavities with increasing \dot{m}_{air} . For the same pore size (PPI), SiSiC cavities achieved higher temperatures than their alumina counterparts, except for a few \dot{m}_{air} values, where $T_{\text{air,out}}$ for alumina 10 PPI was nearly similar to that of SiSiC 10 PPI. At these low \dot{m}_{air} , temperatures for SiSiC 30 PPI were generally lower than those for SiSiC 10 PPI, which in turn were lower than those for 20 PPI. The trend is clearer for the alumina cavities: 10 PPI performed distinctly better than 20 PPI, which in turn performed better than 30 PPI. Fig. 9(b) shows that the highest η_{receiver} of about 0.66 was achieved by SiSiC 10 PPI at $T_{\text{air,out}} = 960$ °C and $\dot{m}_{\text{air}} = 9.5$ kg/h, and by SiSiC 30 PPI at $T_{\text{air,out}} = 914$ °C and $\dot{m}_{\text{air}} = 10$ kg/h. Similar to Fig. 7 and Fig. 8, at the highest $T_{\text{air,out}} = 1095$ °C, η_{receiver} approached 0.30.

For $C = 3900$ suns (Fig. 10(a)), the highest value of C , $T_{\text{air,out}}$ for all the cavities was higher than 1000 °C for the entire range of \dot{m}_{air} (except for a single data point of ceria 10 PPI at 981 °C), with the highest $T_{\text{air,out}} = 1163$ °C by the ceria 10 PPI cavity at $\dot{m}_{\text{air}} = 5.2$ kg/h as well as at 5.87 kg/h. These experiments were started from \dot{m}_{air} of about 4.5 kg/h

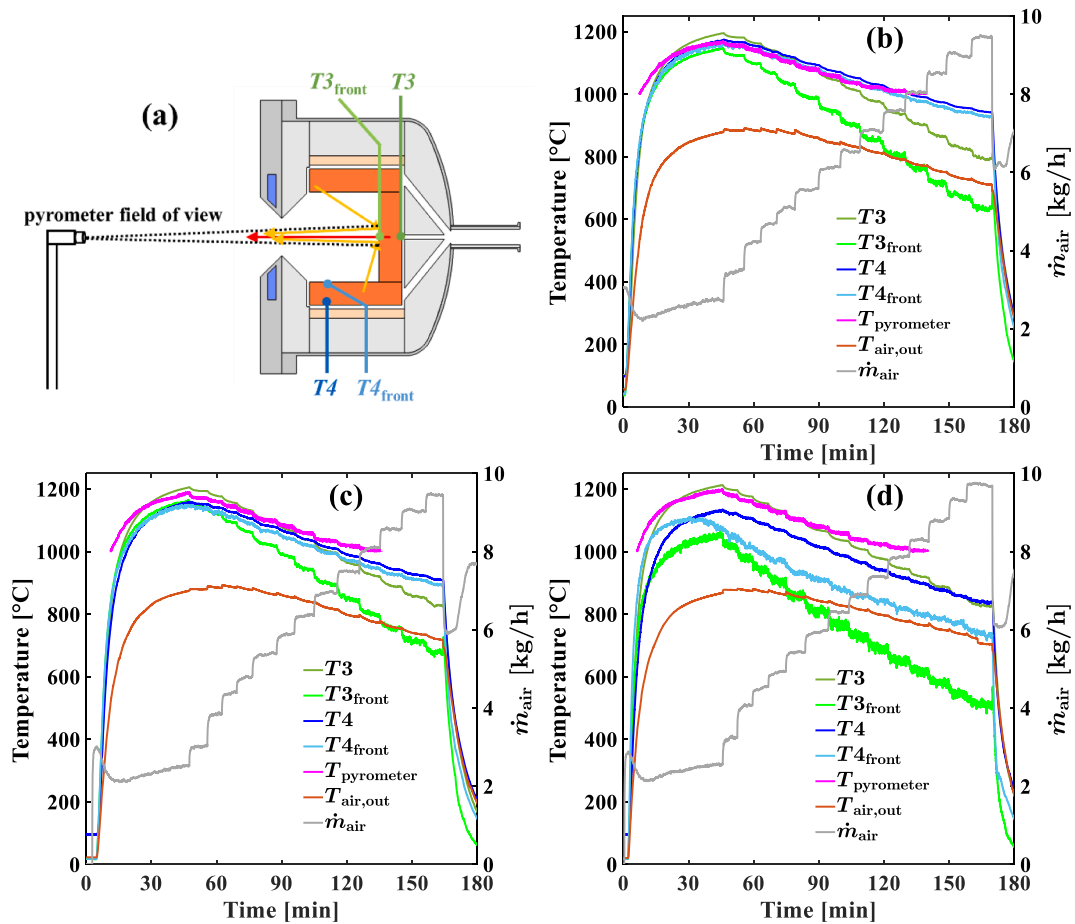


Fig. 12. (a) Schematic of solar receiver setup with the additional thermocouples $T3_{front}$ and $T4_{front}$, and the pyrometer, for the repeated experimental runs with SiSiC RPC cavities at $C = 2475$ suns. Temporal variation of temperatures and \dot{m}_{air} for (b) SiSiC 10 PPI, (c) SiSiC 20 PPI and (d) SiSiC 30 PPI cavities.

(instead of about 2.5 kg/h for the aforementioned experiments with lower C) to prevent overheating of the RPCs. While comparing the different cavities from Fig. 10(a), it is important to note that the maximum relative difference between any two $T_{air,out}$ values (even at dissimilar \dot{m}_{air}) is less than 16%, which is a significantly narrower range compared to lower C levels. In terms of RPC materials, ceria 10 PPI repeated the aforementioned behavior of reaching the highest $T_{air,out}$ at the lower flow rates and falling sharply across $T_{air,out}$ of all other cavities as the flow rate increased. For the same pore size, SiSiC distinctly outperformed alumina. Among the SiSiC cavities, 10 PPI performed best, followed by 20 PPI and 30 PPI. Among the alumina cavities, 10 PPI performed the best, while 20 and 30 PPI performed nearly similarly. Fig. 10(b) shows that $\eta_{receiver}$ peaked at about 0.69 for SiSiC 10 PPI at $T_{air,out} = 1133$ °C and $\dot{m}_{air} = 9.9$ kg/h. At the highest $T_{air,out} = 1163$ °C, $\eta_{receiver}$ approached 0.35. Larger pore sizes yielded better performance than smaller pores at this high C level.

The temperature gradient in the RPC cavity is characterized in Fig. 11(a-d), which shows the maximum difference between any two measurements by thermocouples $T1$ to $T5$ (denoted by ΔT_{RPC}) as a function of \dot{m}_{air} for the seven tested RPC cavities with the four C inputs 1965, 2475, 3230 and 3900 suns. These temperatures were recorded at the same time instance as the corresponding steady-state $T_{air,out}$ measurement in Figs. 7-10. Note that in Fig. 11(c) and 11(d), values of ΔT_{RPC} are omitted for experiments with SiSiC 20 PPI and SiSiC 30 PPI because of thermocouple malfunction. It is found that the SiSiC cavities consistently showed lower ΔT_{RPC} values compared to the alumina cavities. This could be a consequence of the significantly higher solid (and hence effective) thermal conductivity of SiSiC compared to alumina (Fig. 4), which diffuses the hotspots and homogenizes the temperature across the

RPC. Comparing different pore sizes within the same material, there is no clear trend, although at lower \dot{m}_{air} , the largest pore size (10 PPI) tends to have the lowest ΔT_{RPC} , which could be attributed to better redistribution of incident solar radiation and thermal emission from the RPC. The highest ΔT_{RPC} values of up to 500 °C were observed for the lowest $C = 1965$ suns. Such large temperature gradients are attributed to asymmetry of I_{solar} around the cavity axis caused by the use of only three arc lamps. The range of ΔT_{RPC} values shrinks to about 50–250 °C, as C (hence number of arc lamps used) increases and the incident flux distribution becomes more homogenous. With increasing \dot{m}_{air} , ΔT_{RPC} generally increases, even though the absolute RPC temperatures decrease as the receiver cools down with increasing \dot{m}_{air} . Based on the measurements of RPC thermocouples $T1$ - $T5$, it appears that certain parts of the cavity were cooled better than the others, which indicates non-uniform flow and possibly the influence of arc-lamp hotspots as well. Such large temperature gradients in the RPC, especially at high \dot{m}_{air} , are undesired and can in principle be avoided by designing porous structures with variable porosity/pore size in the direction of incident radiation (Capuano et al., 2017; Hoes et al., 2019; Luque et al., 2018). It is important to distinguish this ΔT_{RPC} from the local temperature difference between the RPC and the air, which does decrease with increasing \dot{m}_{air} , as seen from the values of $T1$ - $T5$ and $T_{air,out}$ in the representative experimental run shown in Fig. 6.

RPC temperatures of the three SiSiC cavities were further investigated by repeating their experiments with $C = 2475$ suns. Three additional instruments were used in the repeated runs, as shown schematically in Fig. 12(a). Two thermocouples were inserted on the RPC's inner periphery in front of $T3$ and $T4$, termed $T3_{front}$ and $T4_{front}$. The thermocouple probes of wire diameter 0.35 mm were positioned

approximately 3 mm under the irradiated RPC surface and were thus assumed to be shielded from direct irradiation by the arc lamps. A pyrometer targeting the aperture was employed to measure the cavity's nominal temperature ($T_{\text{pyrometer}}$). Fig. 12(b-d) plots $T_{3\text{front}}$, $T_{4\text{front}}$, T_3 , T_4 , $T_{\text{pyrometer}}$, and $T_{\text{air,out}}$, as well as \dot{m}_{air} as a function of time for the repeated experiments with the SiSiC 10, 20 and 30 PPI cavities. Three major observations can be drawn from the results: 1) For all three SiSiC cavities, $T_{3\text{front}}$ and $T_{4\text{front}}$ were lower than T_3 and T_4 , respectively. This is counter-intuitive because the temperature at the directly irradiated ('front') surface of an RPC with uniform porosity is expected to be higher than that at the rear, given that most of the incident radiation is absorbed in the first few millimeters following Bouguer's law of exponential decay (attenuation). The lower temperature measurements at the front, compared to rear, are attributed to convective cooling by the relatively cold air flow as it impinges at the RPC front. 2) Furthermore, the difference between T_3 and $T_{3\text{front}}$, which are positioned directly upstream of the central exit channel, increased with \dot{m}_{air} , due to increased convective heat transfer by the incoming cold air with increasing \dot{m}_{air} . Uncertainties in these measurements include thermocouples that might not be in contact with the RPC's struts and therefore measuring the air flow temperature. 3) $T_{\text{pyrometer}}$ closely followed T_3 and T_4 within a range of 50 °C (which represents a relative difference of less than 5%) at all \dot{m}_{air} for all three SiSiC cavities. $T_{\text{pyrometer}}$ can be a useful metric to estimate the re-radiation losses through the aperture but cannot capture the information on the temperature distribution inside the cavity, parts of which were at a higher temperature than $T_{\text{pyrometer}}$. Pyrometer readings below 1000 °C were excluded from the plots, as it is not designed to measure below this temperature. In terms of $T_{\text{air,out}}$, the three SiSiC cavities performed similarly as in the runs of Fig. 8 and Fig. 11(b) for $C = 2475$ suns.

Discussion of overall results – The volumetric effect of the solar receiver design becomes evident under certain conditions when comparing the air outlet temperature with the RPC front temperatures. For the SiSiC 30 PPI cavity (Fig. 12(d)), at high \dot{m}_{air} values (between 6.9 and 9.7 kg/h), $T_{\text{air,out}}$ values were greater than the average of $T_{3\text{front}}$ and $T_{4\text{front}}$ by about 18–91 °C. It is worth noting that $T_{\text{air,out}}$ was measured roughly 10 cm downstream of the rear edge of the RPC cavity and still exceeded the average RPC front temperatures. This behavior was observed prominently for the 30 PPI cavity, which had about 3.1 and 1.6 times the surface area of the 10 PPI and 20 PPI cavities, respectively. This indicates the importance of convective heat exchange together with volumetric radiation absorption to achieve the volumetric effect. Incident concentrated radiation penetrates the RPC and undergoes attenuation following Bouguer's law exponential decay. This volumetric absorption is exploited by the HTF flowing across the RPC and being effectively heated by convective exchange occurring within the RPC's volume with a relatively high specific surface area (see Table 1). In terms of radiation attenuation, Monte Carlo ray-tracing analysis at the pore-scale on the exact 3D digital geometry obtained by computer tomography of RPC samples with 10, 20 and 30 PPI indicated values of the effective extinction coefficient of around 247, 480 and 804 m^{-1} , respectively (Table 1) (Ackermann et al., 2017). Recent studies on hierarchically ordered porous structures with a porosity gradient exhibited a step-wise radiative attenuation that lead to a more uniform temperature distribution across the structure (Hoes et al., 2019).

For the same pore size, SiSiC cavities performed better than the corresponding alumina cavities, attributed to the higher thermal conductivity of SiSiC. For SiSiC cavities, there was no prominent trend with respect to the pore size: 10 and 20 PPI performed similarly at $C = 1965$ suns, all three pore sizes performed similarly at $C = 2475$ suns, the trend at $C = 3230$ suns was mixed and lastly, at $C = 3900$ suns, larger pores performed better than smaller ones. On the other hand, for the alumina cavities, the 10 PPI (larger pores) performed better than 20 and 30 PPI across all C levels. However, this trend was not followed when comparing the 20 and 30 PPI. The lack of a prominent trend between the pore sizes across different C levels indicates the presence of competing

effects between radiation, convection and conduction heat transfer. Most of the past parametric studies on RPC absorbers (experimental, numerical or combined) indicate that higher pore densities (i.e. smaller pore sizes, in the range of 1–2 mm or smaller) achieve better performance owing to improved convective heat transfer (Mey-Cloutier et al., 2016; Wang et al., 2020; Wu et al., 2011; Zaversky et al., 2018), while some indicate that larger pores (~4 mm) are more suitable owing to improved radiation heat transfer (Kribus et al., 2014). However, this study placed the absorbers inside a cavity and used much higher mean solar concentration ratios and resulting RPC temperatures compared to the past studies. Differences in performance due to pore size may have been diminished by multiple internal reflections of the incident solar radiation and thermal re-emission by the RPCs (cavity effect). Thermal conductivity is an additional important property, given the more homogenous temperature distribution exhibited by SiSiC RPC cavities relative to alumina (Fig. 11). Finally, convective heat transfer is strongly dependent on the flow characteristics across the porous structures, especially its uniformity, which in turn affect the temperature distributions. Overall, the larger pore size of 10 PPI (~2.5 mm mean pore diameter) tends to provide an advantage over smaller pores for conditions $C > 3000$ suns and $T_{\text{air,out}} > 1000$ °C, which may be expected given the important role of radiation exchange at such high flux intensities and re-emission temperatures.

5. Summary and conclusions

An experimental investigation was conducted with a solar receiver featuring an open cavity containing RPC bricks directly exposed to concentrated solar radiation and using air as the heat transfer fluid. Steady-state air outlet temperatures $T_{\text{air,out}}$ ranging from 1160 to 450 °C were achieved at \dot{m}_{air} between 2 and 10 kg/h for C between 1965 and 3900 suns, resulting in receiver thermal efficiencies η_{receiver} between 0.22 and 0.69. For the same pore size, SiSiC performed better than alumina in terms of $T_{\text{air,out}}$, attributed to its higher thermal conductivity and surface absorptivity for solar radiation. Ceria, which was tested only with 10 PPI pore size, achieved the highest $T_{\text{air,out}}$ out of all the cavities at every flux intensity but only at low \dot{m}_{air} (i.e. at high $T_{\text{air,out}}$). Ceria $T_{\text{air,out}}$ values dropped steeply with increasing \dot{m}_{air} because of air bypassing the RPC structure via gaps created by imperfect machining. There was no prominent trend between the three different pore sizes of SiSiC material across different C levels, presumably due to the effect of the cavity on the interplay between radiation, convection and conduction heat transfer. However, the results indicate that the larger pores of 10 PPI (~2.5 mm mean pore diameter) tend to be beneficial for the low-conducting alumina material and for both materials under conditions of high C (>3000 suns) and $T_{\text{air,out}}$ (>1000 °C) due to the dominant role of radiation heat transfer across the cavity. At the highest $C = 3230$ suns, $T_{\text{air,out}}$ values were consistently higher than 1000 °C for all \dot{m}_{air} . Increasing the \dot{m}_{air} from roughly 4 to 11 kg/h decreased the steady-state $T_{\text{air,out}}$ only by about 12%, while nearly doubling the η_{receiver} to 0.69. Main sources of irreversibility were due to re-radiation through the cavity's aperture, conduction through the insulating walls and temperature gradients of up to 500 °C across the RPC cavity, indicating a considerable scope for optimizing the design for maximum η_{receiver} . The results of this experimental study will be further used to validate a heat transfer and fluid flow model for design optimization and scale-up. The solar air receiver design is simple, robust, and scalable owing to its modularity, and can be directly integrated with a thermochemical-based heat storage, enabling the round-the-clock delivery of heat for high-temperature thermal and thermochemical industrial applications.

Declaration of Competing Interest

The authors declare that they have no known competing financial interests or personal relationships that could have appeared to influence the work reported in this paper.

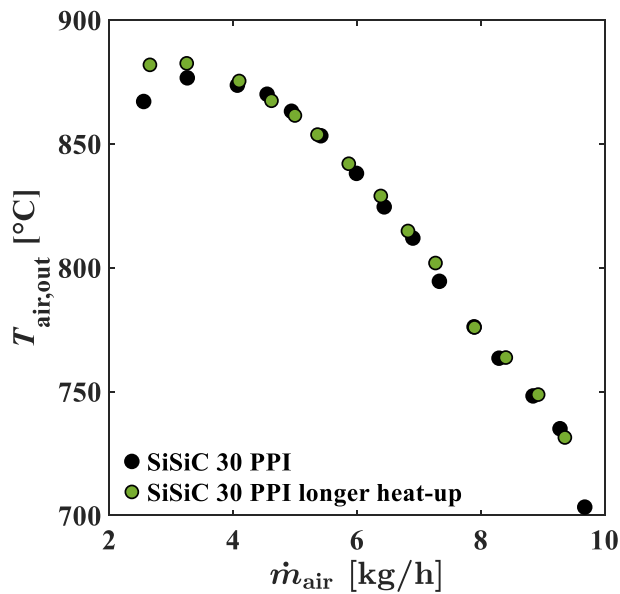


Fig. A1. Repeated experimental run with SiSiC 30 PPI cavity, 3.1 kW power input ($C = 2475$ suns) and 50 mins of additional heat-up time to verify repeatability of measurements and to check the effect of additional heat-up time on initial values of $T_{\text{air,out}}$.

Acknowledgements

We gratefully acknowledge the financial support by the Swiss State

Appendix A. Repeated experiment with longer heat-up time

The experimental run with SiSiC 30 PPI cavity and 3.1 kW power input ($C = 2475$ suns) was repeated in order to serve two purposes: (i) to verify repeatability of the experiments, and (ii) to confirm the hypothesis that the increase in steady-state $T_{\text{air,out}}$ (instead of decrease) with increasing \dot{m}_{air} observed at the start of all experiments was due to transient heating of the insulation. The definition of steady-state (<1% change in 5 min) was applied to $T_{\text{air,out}}$ only, and not to the insulation temperatures, in order to complete the experiments in a reasonable amount of time. $T_{\text{air,out}}$ is expected to attain steady-state faster than the temperature of the insulation around the RPC cavity. As a consequence, at the start of the experiment (i.e. at the lowest \dot{m}_{air}), a higher proportion of heat is expected to flow into the cavity walls for sensible heating of the insulation, curtailing the value of $T_{\text{air,out}}$ measured. An additional 50 min of heat-up time was allowed at the start of the repeated run. The first steady-state $T_{\text{air,out}}$ (i.e. at the lowest \dot{m}_{air}) was higher by nearly 15 °C than the first steady-state $T_{\text{air,out}}$ of the original experiment, while the remaining steady-state $T_{\text{air,out}}$ values were identical (Fig. A1).

Appendix B. Error estimation of $T_{\text{air, out}}$ and η_{receiver}

The error in the air outlet temperature was calculated as a combination of the errors of associated measuring instruments:

$$\delta T_{\text{air,out}} = \sqrt{\delta TC_{\text{air,out}}^2 + \delta NI_{9213}^2} \quad (\text{A2.1})$$

where $\delta T_{\text{air,out}}$, $\delta TC_{\text{air,out}}$ and δNI_{9213} are the standard deviations of $T_{\text{air,out}}$, the air outlet thermocouple and the NI 9213 thermocouple input module, respectively. Similar error calculation was applied for the receiver efficiency.

$$\eta_{\text{receiver}} = \frac{P_{\text{air,out}}}{P_{\text{solar}}} = \frac{\dot{m}_{\text{air}} \int_{T_{\text{air,in}}}^{T_{\text{air,out}}} C_{p,\text{air}}(T) dT}{\dot{V}_{\text{water}} \rho_{\text{water}} C_{p,\text{water}} \Delta T_{\text{water}}} \quad (\text{A2.2})$$

where \dot{V}_{water} , ρ_{water} , $C_{p,\text{water}}$ and ΔT_{water} are the volumetric flow rate, density, specific heat capacity and temperature gain of the water flowing across the calorimeter used to measure P_{solar} .

References

- Ackermann, S., Steinfeld, A., 2017. Spectral hemispherical reflectivity of nonstoichiometric cerium dioxide. *Sol. Energy Mater. Sol. Cells* 159, 167–171. <https://doi.org/10.1016/j.solmat.2016.08.036>.
- Ackermann, S., Takacs, M., Scheffe, J., Steinfeld, A., 2017. Reticulated porous ceria undergoing thermochemical reduction with high-flux irradiation. *Int. J. Heat Mass Transf.* 107, 439–449. <https://doi.org/10.1016/j.ijheatmasstransfer.2016.11.032>.
- Agrafiotis, C., Mavroidis, I., Konstandopoulos, A., Hoffschmidt, B., Stobbe, P., Romero, M., Fernandezquero, V., 2007. Evaluation of porous silicon carbide monolithic honeycombs as volumetric receivers/collectors of concentrated solar

- radiation. *Sol. Energy Mater. Sol. Cells* 91, 474–488. <https://doi.org/10.1016/j.solmat.2006.10.021>.
- Albanakis, C., Missirlis, D., Michailidis, N., Yakinthos, K., Goulas, A., Omar, H., Tsipas, D., Granier, B., 2009. Experimental analysis of the pressure drop and heat transfer through metal foams used as volumetric receivers under concentrated solar radiation. *Exp. Therm. Fluid Sci.* 33, 246–252. <https://doi.org/10.1016/j.expthermflusci.2008.08.007>.
- Ávila-Marín, A.L., 2011. Volumetric receivers in Solar Thermal Power Plants with Central Receiver System technology: A review. *Sol. Energy* 85, 891–910. <https://doi.org/10.1016/j.solener.2011.02.002>.
- Ávila-Marín, A.L., Alvarez-Lara, M., Fernandez-Reche, J., 2014. Experimental Results of Gradual Porosity Wire Mesh Absorber for Volumetric Receivers. *Energy Procedia* 49, 275–283. <https://doi.org/10.1016/j.egypro.2014.03.030>.
- Ávila-Marín, A.L., Alvarez de Lara, M., Fernandez-Reche, J., 2018. Experimental results of gradual porosity volumetric air receivers with wire meshes. *Renew. Energy* 122, 339–353. <https://doi.org/10.1016/j.renene.2018.01.073>.
- Battleson, K.W., 1981. Solar power tower design guide: solar thermal central receiver power systems, a source of electricity and/or process heat. Albuquerque, NM, and Livermore, CA (United States). doi: 10.12172/6335255.
- Blanco, M.J., Miller, S., 2017. Introduction to concentrating solar thermal (CST) technologies, in: *Advances in Concentrating Solar Thermal Research and Technology*. Elsevier, pp. 3–25. doi: 10.1016/B978-0-08-100516-3.00001-0.
- Buck, R., Bräuning, T., Denk, T., Pfänder, M., Schwarzbözl, P., Tellez, F., 2002. Solar-Hybrid Gas Turbine-based Power Tower Systems (REFOS). *J. Sol. Energy Eng.* 124, 2–9. <https://doi.org/10.1115/1.1445444>.
- Buck, R., Muir, J.F., Hogan, R.E., Skocypec, R.D., 1991. Carbon dioxide reforming of methane in a solar volumetric receiver/reactor: the CAESAR project. *Sol. Energy Mater.* 24, 449–463. [https://doi.org/10.1016/0165-1633\(91\)90082-V](https://doi.org/10.1016/0165-1633(91)90082-V).
- Capuano, R., Fend, T., Stadler, H., Hoffschmidt, B., Pitz-Paal, R., 2017. Optimized volumetric solar receiver: Thermal performance prediction and experimental validation. *Renew. Energy* 114, 556–566. <https://doi.org/10.1016/j.renene.2017.07.071>.
- Chavez, J.M., Chaza, C., 1991. Testing of a porous ceramic absorber for a volumetric air receiver. *Sol. Energy Mater.* 24, 172–181. [https://doi.org/10.1016/0165-1633\(91\)90057-R](https://doi.org/10.1016/0165-1633(91)90057-R).
- Eyring, V., Köhler, H.W., Lauer, A., Lemper, B., 2005. Emissions from international shipping: 2. Impact of future technologies on scenarios until 2050. *J. Geophys. Res.* 110, D17306. <https://doi.org/10.1029/2004JD005620>.
- Fend, T., Hoffschmidt, B., Pitz-Paal, R., Reutter, O., Rietbrock, P., 2004. Porous materials as open volumetric solar receivers: Experimental determination of thermophysical and heat transfer properties. *Energy* 29, 823–833. [https://doi.org/10.1016/S0360-5442\(03\)00188-9](https://doi.org/10.1016/S0360-5442(03)00188-9).
- Furler, P., Scheffe, J., Gorbar, M., Moes, L., Vogt, U., Steinfeld, A., 2012. Solar Thermochemical CO₂ Splitting Utilizing a Reticulated Porous Ceria Redox System. *Energy Fuels* 26, 7051–7059. <https://doi.org/10.1021/ef3013757>.
- Gianella, S., Gaia, D., Ortona, A., 2012. High temperature applications of Si-SiC cellular ceramics. *Adv. Eng. Mater.* 14, 1074–1081. <https://doi.org/10.1002/adem.201200012>.
- Gigantino, M., Sas Brunser, S., Steinfeld, A., 2020. High-Temperature Thermochemical Heat Storage via the CuO/Cu₂O Redox Cycle: From Material Synthesis to Packed-Bed Reactor Engineering and Cyclic Operation. *Energy Fuels*. <https://doi.org/10.1021/acs.energyfuels.0c02572>.
- Gomez-García, F., González-Aguilar, J., Olalde, G., Romero, M., 2016a. Thermal and hydrodynamic behavior of ceramic volumetric absorbers for central receiver solar power plants: A review. *Renew. Sustain. Energy Rev.* 57, 648–658. <https://doi.org/10.1016/j.rser.2015.12.106>.
- Gomez-García, F., Santiago, S., Luque, S., Romero, M., Gonzalez-Aguilar, J., 2016b. A new laboratory-scale experimental facility for detailed aerothermal characterizations of volumetric absorbers, in: *AIP Conference Proceedings* 1734. p. 030018. doi: 10.1063/1.4949070.
- Grote, M., Williams, I., Preston, J., 2014. Direct carbon dioxide emissions from civil aircraft. *Atmos. Environ.* 95, 214–224. <https://doi.org/10.1016/j.atmosenv.2014.06.042>.
- Hausseiner, S., Coray, P., Lipiński, W., Wyss, P., Steinfeld, A., 2010. Tomography-Based Heat and Mass Transfer Characterization of Reticulate Porous Ceramics for High-Temperature Processing. *ASME J. Heat Transf.* 132 (023305), 1–9. <https://doi.org/10.1115/1.4000226>.
- Hischier, I., Leumann, P., Steinfeld, A., 2012. Experimental and numerical analyses of a pressurized air receiver for solar-driven gas turbines. doi: 10.1115/1.4005446.
- Ho, C.K., 2017. Advances in central receivers for concentrating solar applications. *Sol. Energy* 152, 38–56. <https://doi.org/10.1016/j.solener.2017.03.048>.
- Ho, C.K., Iverson, B.D., 2014. Review of high-temperature central receiver designs for concentrating solar power. *Renew. Sustain. Energy Rev.* 29, 835–846. <https://doi.org/10.1016/j.rser.2013.08.099>.
- Hoes, M., Ackermann, S., Theiler, D., Furler, P., Steinfeld, A., 2019. Additive-Manufactured Ordered Porous Structures Made of Ceria for Concentrating Solar Applications. *Energy Technol.* 7, 1900484. <https://doi.org/10.1002/ente.201900484>.
- Hoffschmidt, B., Pitz-Paal, R., Böhmer, M., Fend, T., Rietbrock, P., 1999. 200 kWth open volumetric air receiver (HiTRec) of DLR reached 1000°C average outlet temperature at PSA. *J. Phys. IV Fr.* 9, 551–556. <https://doi.org/10.1051/jp4:1999387>.
- International Energy Agency, 2020. Tracking Industry 2020 – Analysis [WWW Document]. URL <https://www.iea.org/reports/tracking-industry-2020> (accessed 7.8.20).
- Karni, J., Kribus, A., Doron, P., Rubín, R., Fiterman, A., Sagie, D., 1997. The DIAPR: A high-pressure, high-temperature solar receiver. *J. Sol. Energy Eng. Trans. ASME* 119, 74–78. <https://doi.org/10.1115/1.2871853>.
- Karni, J., Kribus, A., Ostrach, B., Kochavi, E., 1998. A High-Pressure Window for Volumetric Solar Receivers. *J. Sol. Energy Eng.* 120, 101–107. <https://doi.org/10.1115/1.2888051>.
- Kribus, A., Doron, P., Rubín, R., Reuven, R., Taragan, E., Duchan, S., Karni, J., 2001. Performance of the Directly-Irradiated Annular Pressurized Receiver (DIAPR) operating at 20 bar and 1200°C. *J. Sol. Energy Eng. Trans. ASME* 123, 10–17. <https://doi.org/10.1115/1.1345844>.
- Kribus, A., Gray, Y., Grijnevich, M., Mittelman, G., Mey-Cloutier, S., Caliot, C., 2014. The promise and challenge of solar volumetric absorbers. *Sol. Energy* 110, 463–481. <https://doi.org/10.1016/j.solener.2014.09.035>.
- Leuchsner, V., 1991. The PLVCR 500 and HCPC, tests and results, NASA STI/Recon Technical Report N. 94.
- Li, Q., Zhang, Q., 2020. Experimental study on the influence of input solar flux, air flow rate, and absorber parameters on honeycomb ceramic air receiver performance. *J. Renew. Sustain. Energy* 12, 023701. <https://doi.org/10.1063/1.5142805>.
- Luque, S., Menéndez, G., Roccabruna, M., González-Aguilar, J., Crema, L., Romero, M., 2018. Exploiting volumetric effects in novel additively manufactured open solar receivers. *Sol. Energy* 174, 342–351. <https://doi.org/10.1016/j.solener.2018.09.030>.
- Marxer, D., Furler, P., Takacs, M., Steinfeld, A., 2017. Solar thermochemical splitting of CO₂ into separate streams of CO and O₂ with high selectivity, stability, conversion, and efficiency. *Energy Environ. Sci.* 10, 1142–1149. <https://doi.org/10.1039/C6EE03776C>.
- Mey-Cloutier, S., Caliot, C., Kribus, A., Gray, Y., Flamant, G., 2016. Experimental study of ceramic foams used as high temperature volumetric solar absorber. *Sol. Energy* 136, 226–235. <https://doi.org/10.1016/j.solener.2016.06.066>.
- Nathan, G.J., Suenaga, M., Kodama, T., Tourbier, D., Zughbi, H., Dally, B.B., Stechel, E. B., Sattler, C., Cochrane, D., DeGaris, R., Lovegrove, K., Hooley, L., Jeanes, S., Metha, G.F., Arjomandi, M., Matthews, C., 2019. HiTEMP Outlook 2018. Transforming High Temperature Minerals Processing: A multi-stakeholder perspective on pathways to high value, net-zero CO₂ products for the new economy.
- Ortona, A., Trimis, D., Uhlir, V., Eder, R., Gianella, S., Fino, P., D'Amico, G., Boulet, E., Chazelas, C., Grämer, T., Cresci, E., Wünnig, J.G., Altena, H., Beneke, F., Debier, M., 2014. SiSiC Heat Exchangers for Recuperative Gas Burners with Highly Structured Surface Elements. *Int. J. Appl. Ceram. Technol.* 11, 927–937. <https://doi.org/10.1111/ijac.12087>.
- Pabst, C., Feckler, G., Schmitz, S., Smirnova, O., Capuano, R., Hirth, P., Fend, T., 2017. Experimental performance of an advanced metal volumetric air receiver for Solar Towers. *Renew. Energy* 106, 91–98. <https://doi.org/10.1016/j.renene.2017.01.016>.
- Parrodi, J.C.H., Lucas, H., Gigantino, M., Sauve, G., Esguerra, J.L., Einhäupl, P., Vollprecht, D., Pomberger, R., Friedrich, B., Van Acker, K., Krook, J., Svensson, N., Van Passel, S., 2019. Integration of resource recovery into current waste management through (Enhanced) landfill mining. *Detritus* 8–2019, 141–156.
- Petrash, J., Meier, F., Friess, H., Steinfeld, A., 2008. Tomography based determination of permeability, Dupuit-Forchheimer coefficient, and interfacial heat transfer coefficient in reticulate porous ceramics. *Int. J. Heat Fluid Flow* 29, 315–326. <https://doi.org/10.1016/j.ijheatfluidflow.2007.09.001>.
- Petrash, J., Wyss, P., Steinfeld, A., 2007. Tomography-based Monte Carlo determination of radiative properties of reticulate porous ceramics. *J. Quant. Spectrosc. Radiat. Transf.* 105, 180–197. <https://doi.org/10.1016/j.jqsrt.2006.11.002>.
- Potamias, D., Alxneit, I., Koepf, E., Wokaun, A., 2019. Double Modulation Pyrometry Applied to Radiatively Heated Surfaces With Dynamic Optical Properties. *J. Sol. Energy Eng.* 141, 1–8. <https://doi.org/10.1115/1.4040842>.
- Pozivil, P., Ettlin, N., Stucker, F., Steinfeld, A., 2015. Modular design and experimental testing of a 50 kWth pressurized-air solar receiver for gas turbines. *J. Sol. Energy Eng. Trans. ASME* 137. <https://doi.org/10.1115/1.4028918>.
- Pritzkow, W.E.C., 1991. Pressure loaded volumetric ceramic receiver. *Sol. Energy Mater.* 24, 498–507. [https://doi.org/10.1016/0165-1633\(91\)90086-Z](https://doi.org/10.1016/0165-1633(91)90086-Z).
- Purdue University. Thermophysical Properties Research Center, 1967. Thermophysical Properties of High Temperature Solid Materials: Oxides and their solutions and mixtures. Solutions and their mixtures of simple oxygen compounds, including glasses and ceramic glasses / Y.S. Touloukian, editor. Macmillan.
- Röger, M., Pfänder, M., Buck, R., 2006. Multiple Air-Jet Window Cooling for High-Temperature Pressurized Volumetric Receivers: Testing, Evaluation, and Modeling. *J. Sol. Energy Eng.* 128, 265–274. <https://doi.org/10.1115/1.2212437>.
- Romero, M., González-Aguilar, J., 2017. Next generation of liquid metal and other high-performance receiver designs for concentrating solar thermal (CST) central tower systems, in: *Advances in Concentrating Solar Thermal Research and Technology*. Elsevier, pp. 129–154. doi: 10.1016/B978-0-08-100516-3.00007-1.
- Romero, M., Gonzalez-Aguilar, J., Sizmann, A., Batteiger, V., Steinfeld, A., Zoller, S., Brendelberger, S., Lieftink, D., 2019. Solar-Driven Thermochemical Production of Sustainable Liquid Fuels from H₂O and CO₂ in a Helioast Field, in: *Proceedings of the ISES Solar World Congress 2019*. Solar World Congress, 04–07. Nov. 2019, Santiago, Chile.
- Romero, M., Steinfeld, A., 2012. Concentrating solar thermal power and thermochemical fuels. *Energy Environ. Sci.* 5, 9234–9245. <https://doi.org/10.1039/c2ee21275g>.
- Sedighi, M., Padilla, R.V., Taylor, R.A., Lake, M., Izadgoshasb, I., Rose, A., 2019. High-temperature, point-focus, pressurized gas-phase solar receivers: A comprehensive review. *Energy Convers. Manag.* <https://doi.org/10.1016/j.enconman.2019.02.020>.
- von Storch, H., Roeb, M., Stadler, H., Sattler, C., Hoffschmidt, B., 2016. Efficiency potential of indirectly heated solar reforming with different types of solar air receivers. *Appl. Therm. Eng.* 92, 202–209. <https://doi.org/10.1016/j.applthermaleng.2015.09.065>.

- Wang, P., Li, J.B., Zhou, L., Vafai, K., 2020. Experimental characterization on pore parameter and the irradiation absorption efficiency of a series SiC foam specimens. *Energy Convers. Manag.* 212, 112795 <https://doi.org/10.1016/j.enconman.2020.112795>.
- Wu, Z., Caliot, C., Flamant, G., Wang, Z., 2011. Coupled radiation and flow modeling in ceramic foam volumetric solar air receivers. *Sol. Energy* 85, 2374–2385. <https://doi.org/10.1016/j.solener.2011.06.030>.
- Zanganeh, G., Pedretti, A., Zavattoni, S., Barbato, M., Steinfeld, A., 2012. Packed-bed thermal storage for concentrated solar power – Pilot-scale demonstration and industrial-scale design. *Sol. Energy* 86, 3084–3098. <https://doi.org/10.1016/j.solener.2012.07.019>.
- Zaversky, F., Aldaz, L., Sánchez, M., Ávila-Marín, A.L., Roldán, M.I., Fernández-Reche, J., Füssel, A., Beckert, W., Adler, J., 2018. Numerical and experimental evaluation and optimization of ceramic foam as solar absorber – Single-layer vs multi-layer configurations. *Appl. Energy* 210, 351–375. <https://doi.org/10.1016/j.apenergy.2017.11.003>.
- Zaversky, F., Aldaz, L., Sánchez, M., Fernández-Reche, J., Füssel, A., Adler, J., 2019. Experimental and numerical evaluation of a small array of ceramic foam volumetric absorbers. In: *AIP Conference Proceedings*, p. 030066. <https://doi.org/10.1063/1.5117578>.
- Zaversky, F., Les, I., Sorbet, P., Sánchez, M., Valentin, B., Brau, J.-F., Siros, F., 2020. The challenge of solar powered combined cycles – Providing dispatchability and increasing efficiency by integrating the open volumetric air receiver technology. *Energy* 194, 116796. <https://doi.org/10.1016/j.energy.2019.116796>.